

Probing phase transition of band topology via radiation topology

CHANG-YIN JI,^{1,2,†} WENZE LAN,^{3,4,†} PENG FU,^{3,4} GANG WANG,¹ CHANGZHI GU,^{3,4} YELIANG WANG,² JIAFANG LI,^{1,7}  YUGUI YAO,^{1,8} AND BAOLI LIU^{3,5,6,*}

¹Key Laboratory of Advanced Optoelectronic Quantum Architecture and Measurement (MOE), Beijing Key Laboratory of Nanophotonics & Ultrafine Optoelectronic Systems, and School of Physics, Beijing Institute of Technology, Beijing 100081, China

²School of Integrated Circuits and Electronics, MIIT Key Laboratory for Low-Dimensional Quantum Structure and Devices, Beijing Institute of Technology, Beijing 100081, China

³Beijing National Laboratory for Condensed Matter Physics, Institute of Physics, Chinese Academy of Sciences, Beijing 100190, China

⁴School of Physical Sciences, CAS Key Laboratory of Vacuum Physics, University of Chinese Academy of Sciences, Beijing 100190, China

⁵CAS Center for Excellence in Topological Quantum Computation, CAS Key Laboratory of Vacuum Physics, University of Chinese Academy of Sciences, Beijing 100190, China

⁶Songshan Lake Materials Laboratory, Dongguan 523808, China

⁷e-mail: jiafangli@bit.edu.cn

⁸e-mail: ygyao@bit.edu.cn

[†]These authors contributed equally to this work.

*Corresponding author: blliu@iphy.ac.cn

Received 17 July 2023; revised 8 January 2024; accepted 9 January 2024; posted 9 January 2024 (Doc. ID 500575); published 17 May 2024

Topological photonics has received extensive attention from researchers because it provides brand new physical principles to manipulate light. Band topology is characterized using the Berry phase defined by Bloch states. Until now, the scheme for experimentally probing the topological phase transition of band topology has always been relatively lacking in topological physics. Moreover, radiation topology can be aroused by the far-field polarization singularities of Bloch states, which is described by the Stokes phase. Although such two types of topologies are both related to Bloch states on the band structures, it is rather surprising that their development is almost independent. Here, in optical analogs of the quantum spin Hall effects (QSHEs) and Su-Schrieffer-Heeger model, we reveal the correlation between the phase transition of band topology and radiation topology and then demonstrate that the radiation topology can be employed to study the band topological transition. We experimentally demonstrate such an intriguing phenomenon in optical analogs of QSHEs. Our findings not only provide an insightful understanding of band topology and radiation topology, but also can serve as a route to manipulate light. © 2024 Chinese Laser Press

<https://doi.org/10.1364/PRJ.500575>

1. INTRODUCTION

Topological photonics is an emerging field that provides whole new research perspectives to manipulate the flow of light [1–6]. The band topology in photonics is derived from condensed matter physics [7], which classifies insulators and semimetals into different types. The bulk of photonic topological insulators (PTIs) is still insulating but their boundaries do conduct. Due to the topological protection, the topological states propagated at boundaries of the PTIs are very robust even with imperfections. Such robust unidirectional transport characteristics of the topological states make PTIs striking materials in the applications of optical devices, such as high transmission waveguides [8,9], robust optical delay lines [10], topological lasers [11–13], quantum photonic circuits [14], robust optical switches,

bistable states [15], and nonlinearly induced topologically protected edge state transport [16]. The topological quasiparticles, such as topological exciton-polaritons and phonon-polaritons, can also be obtained by the strong coupling of topological photons with excitons [17,18] and phonons [19]. These aforementioned novel phenomena and applications are attributed to the topological phase transitions of band topology. Thus, it is crucial to accurately characterize the topological properties of optical materials.

In theory, we can characterize the topological property of the bulk physics and its evolution in the parameter space by calculating the topological invariant [20]. This method requires obtaining the Bloch states on the band structures [21], which makes it very difficult to experimentally measure the topological invariant, especially in topological photonics. Currently, an

experimentally feasible approach for probing the topological properties of band structures is to explore the existence of In-GaP topological states in a strip-shaped sample based on the principle of bulk-boundary correspondence [2,22]. However, such method usually requires a full bandgap, which obviously hinders its application to more general situations. For example, the topological states merge with the trivial bulk states when there is not a full bandgap [23–26]. In this case, the spectral measurements alone are not enough; the near-field distribution of the modes is needed to determine whether the state is topological. Moreover, such method is also very difficult to probe the band topological transitions when the topologically inequivalent materials on both sides of the domain wall do not have a common bandgap. This is due to the fact that in this case there may be no topological states on the domain wall. Thus, it is necessary and interesting to find new methods that investigate the band topology; for example, some works propose the spectroscopic means via Fano resonances [27] and introduce crystalline defects in acoustic metamaterials [28,29]. Recently, other works also point out the scattered/reflected field to probe the topological signature of band singularities such as Weyl points [30,31].

When the frequency of the Bloch state (photonic mode) is above the light cone [4–6], the Bloch state can leak into the far field. In such case, one can map the far-field polarization of the radiating Bloch state in the momentum space. The radiation topology can be formed when there are polarization singularities in the momentum space [4–6], which is a class of topological defects. A well-known example of the radiation topology is bound states in the continuum (BICs) [32,33]. Recently, some works investigated the dynamics of radiation topology, whose processes are accompanied by many interesting physical phenomena [34–42]. However, little attention has been paid to the band topological properties when studying the radiative topology of the photonic band structure, and vice versa. The band topology and radiation topology are almost viewed as independent themes in the realm of topological photonics. In fact, such two vibrant topological phenomena are both rooted in the Bloch states on the band structures in photonic crystals. Thus, it is very intriguing to ask whether we can use radiation topology to probe the phase transition of band topology. Their connections can not only lead to our deep understanding of different topological branches, but also provide brand new schemes to manipulate the flow of light at material domain walls and light radiation in the far-field.

Here, in optical analogs of the quantum spin Hall effects (QSHEs) and Su-Schrieffer-Heeger (SSH) model, we discover the correlation between the phase transition of the band topology and radiation topology and then demonstrate that radiation topology can be employed to study the band topological transition. To confirm such idea experimentally, we fabricate photonic crystal slabs (PhCSs) that have the radiation topology and the band topology for optical analogs of the QSHEs. The theoretical results are verified very well by experimental measurements. Our approach may inspire researchers to experimentally discover and realize optical topological materials.

2. RESULTS AND DISCUSSION

When there is no band degeneracy above the light cone and there are also no compatible diffraction channels of the radiating Bloch states, the far-field polarization vector $[\mathbf{c}(\mathbf{k}_{\parallel})]$ of the radiating Bloch states with Bloch wave vector \mathbf{k}_{\parallel} can be obtained by

$$\mathbf{c}(\mathbf{k}_{\parallel}) = \iint_{\text{u.c.}} \mathbf{E}(x, y, z) e^{i(k_x x + k_y y)} dx dy. \quad (1)$$

$\mathbf{E}(x, y, z)$ in Eq. (1) is the electric field distribution. The integration is calculated in one unit cell (u.c.) on an xy plane outside the PhCSs. The state of polarization (SoP) can be described by Stokes parameters (S_0, S_1, S_2, S_3) . Then, we project $\mathbf{c}(\mathbf{k}_{\parallel})$ into the xy plane: $\mathbf{c}_{xy}(\mathbf{k}_{\parallel}) = c_x(\mathbf{k}_{\parallel})\hat{x} + c_y(\mathbf{k}_{\parallel})\hat{y}$, where $c_x(\mathbf{k}_{\parallel}) = \hat{x} \cdot \mathbf{c}(\mathbf{k}_{\parallel})$ and $c_y(\mathbf{k}_{\parallel}) = \hat{y} \cdot \mathbf{c}(\mathbf{k}_{\parallel})$. In such case, the Stokes parameters can be expressed as the following form:

$$\begin{aligned} S_0 &= |c_x(\mathbf{k}_{\parallel})|^2 + |c_y(\mathbf{k}_{\parallel})|^2, \\ S_1 &= |c_x(\mathbf{k}_{\parallel})|^2 - |c_y(\mathbf{k}_{\parallel})|^2, \\ S_2 &= 2 \operatorname{Re}[c_x^*(\mathbf{k}_{\parallel})c_y(\mathbf{k}_{\parallel})], \\ S_3 &= 2 \operatorname{Im}[c_x^*(\mathbf{k}_{\parallel})c_y(\mathbf{k}_{\parallel})]. \end{aligned} \quad (2)$$

The Stokes phase $\phi(\mathbf{k}_{\parallel})$ is expressed as

$$\phi(\mathbf{k}_{\parallel}) = \frac{1}{2} \arg(S_1 + iS_2). \quad (3)$$

Then, one can define topological charge q carried by the polarization singularity:

$$q = \frac{1}{2\pi} \oint_L d\mathbf{k}_{\parallel} \cdot \nabla_{\mathbf{k}_{\parallel}} \phi(\mathbf{k}_{\parallel}), \quad (4)$$

where L is a closed loop around the singular point of polarization in the counterclockwise direction. q is equal to the winding number of $\mathbf{c}_{xy}(\mathbf{k}_{\parallel})$ around singular points for linear polarization.

Now, we show that the phase transition of band topology can be probed by radiation topology for optical analogs of the QSHEs. The designed SiN_x PhCS is shown in the inset of Fig. 1(a) with thickness of $t = 100$ nm and lattice period of $P = 496$ nm (see Fig. 4 in Appendix A), in which the topological properties of the bulk bands are determined by the ratio of P/R [43]. R is the distance from the center of the triangular air hole to the center of the unit cell. This system has the trivial band topology for $P/R > 3$ because the frequency of the odd modes (p orbitals) is lower than that of even modes (d orbitals) at Γ point, whereas the system has the non-trivial band topology for $P/R < 3$ due to the band inversion occurring between odd and even modes; see Fig. 1(g). In addition to changing P/R , we can also control the topological properties of this system by rotating the six triangular air holes. Although such configuration has been widely adopted to investigate the optical analogs of QSHEs, previous works just focus on boundary responses and applications aroused from the band topology [17–19,44–49].

Figure 1(a) is the band structures for $R = 148$ nm with the trivial band topology. There are four transverse electric (TE)-like photonic bands within the considered wavelength

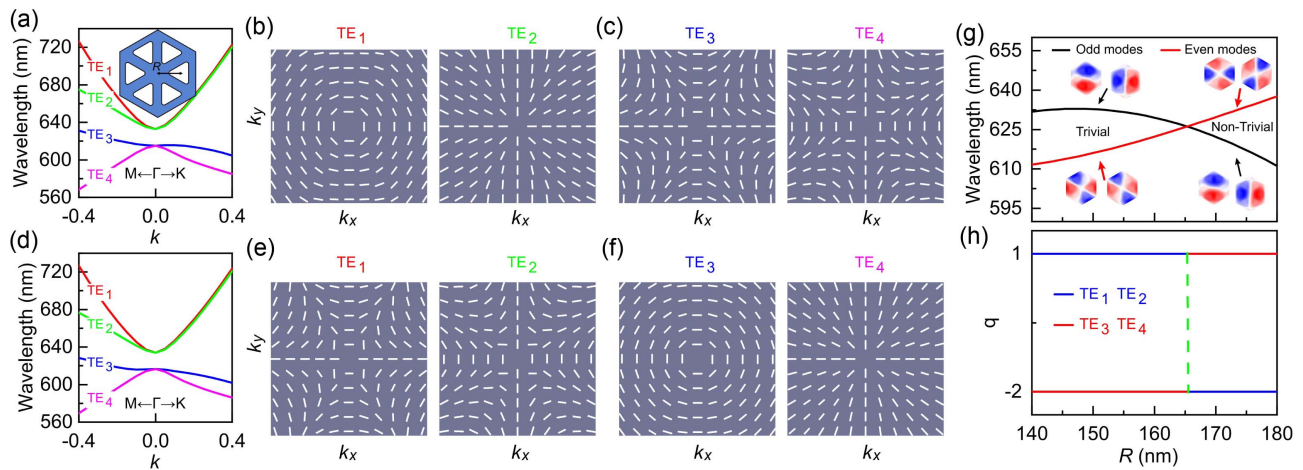


Fig. 1. Probing phase transition of band topology via radiation topology for optical analogs of the QSHEs. The graphene-like SiN_x PhCSs are shown in the inset of (a). R is the distance from the center of the triangular air hole to the center of the unit cell. (a), (d) Calculated transverse electric (TE)-like band structure with $R = 148$ nm in (a) and $R = 175.5$ nm in (d). (b), (c) and (e), (f) Calculated far-field polarization vectors (white lines) around the center of the Brillouin zone for the four photonic bands in (a) and (d), respectively. (g) Illustration of topological phase transition of band topology with R . The insets in (g) are the field distributions of the odd modes and even modes at Γ point for the z component of the magnetic field. (h) Evolution of topological charge q with R . The units of k and k_x (k_y) are $2\pi/P$ and π/P (π/P), respectively. The ranges of k_x and k_y are from -0.1 to 0.1 . The change of q after the band inversion is three for the four bands, while the change of the topological invariant (spin Chern number) of the $\text{TE}_{1/2}$ ($\text{TE}_{3/4}$) band is ± 1 (∓ 1).

range. The far-field polarizations of the radiating Bloch states for the band structures in Fig. 1(a) are shown in Figs. 1(b) and 1(c). Here, the $\mathbf{c}_{xy}(\mathbf{k}_{\parallel})$ is shown by line segments without arrows because one cannot distinguish $\mathbf{c}_{xy}(\mathbf{k}_{\parallel})$ and $-\mathbf{c}_{xy}(\mathbf{k}_{\parallel})$ under temporal harmonic oscillations. It can be seen from Figs. 1(b) and 1(c) that the far-field polarizations are linearly polarized due to the C_2 rotational symmetry and time reversal symmetry. The results in Fig. 1(b) show that the distributions of far-field polarizations for the TE_1 and TE_2 bands are similar to the azimuthally and radially linearly polarized vectorial optical fields (VOFs) in the real space, respectively. Thus, the distributions of $\mathbf{c}_{xy}(\mathbf{k}_{\parallel})$ create a polarization vortex in the momentum space and the center of the vortex is located at Γ point. The value of the topological charge q is equal to $+1$ for the TE_1 and TE_2 bands in Fig. 1(b) deduced from the winding number of $\mathbf{c}_{xy}(\mathbf{k}_{\parallel})$ around Γ point, which can also be confirmed by the corresponding Stokes phase $\phi(\mathbf{k}_{\parallel})$ in Fig. 5 (Appendix A). The distributions of the far-field polarizations in Fig. 1(c) are more complex than that in Fig. 1(b). $c_y(\mathbf{k}_{\parallel})$ is zero along the directions of ΓK and ΓM for the TE_3 band in Fig. 1(c). Based on distributions of $\mathbf{c}_{xy}(\mathbf{k}_{\parallel})$ and Stokes phase, the topological charge is $q = -2$ for the TE_3 band in Fig. 1(c). A similar analysis can be applied to the TE_4 band in Fig. 1(c), which shows that its topological charge is also -2 . Although the band topology is trivial, the radiation topology is indeed non-trivial.

The photonic band structure for $R = 175.5$ nm with the non-trivial band topology is shown in Fig. 1(d), in which the dispersion curves are quite similar to that in Fig. 1(a). The distributions of the far-field polarizations are shown in Figs. 1(e) and 1(f) for the band structures in Fig. 1(d). Interestingly, the results in Fig. 1(e) show that the q is -2

for the TE_1 and TE_2 bands, while the q is $+1$ for the TE_3 and TE_4 bands as shown in Fig. 1(f). This means that when the band topology undergoes a phase transition, the radiation topology also undergoes a topological phase transition. Therefore, this result shows that although the connection between topological properties of band topology and radiation topology may not be obvious, there indeed exists a correlation between their topological phase transition processes.

To confirm this, we further study how their topological properties vary with R . As shown in Fig. 1(h), when R is less than $P/3$, the q of the $\text{TE}_{1/2}$ and $\text{TE}_{3/4}$ bands remains $+1$ and -2 , respectively. However, once R is larger than $P/3$, the q of $\text{TE}_{1/2}$ ($\text{TE}_{3/4}$) bands changes from $+1$ to -2 (from -2 to $+1$). The phase transition critical points for both the band topology and the radiation topology are $R = P/3$, and their phase transitions are both caused by band inversion at the Γ point. In fact, the q is determined by the band representation (symmetry) of the Bloch mode at the high symmetry point [32,50]. Thus, the q does not change unless the band representation changes when the parameter changes do not change the symmetry of the system. Band representation changes often require a bandgap to close and reopen, leading to the phase transitions of band topology. Such observation suggests that one can indeed probe phase transitions of band topology using radiation topology.

Next, we demonstrate theoretically that the radiative topology scheme can probe topological phase transitions of the SSH model [51] implemented in optical systems. We implement the SSH model using a one-dimensional photonic crystal, as shown in the insets of Figs. 2(a) and 6 (Appendix A). The Zak phase is used to characterize the topological properties of the band structures for this system [52]. The Zak phase is a concept in condensed matter physics that is used to describe the

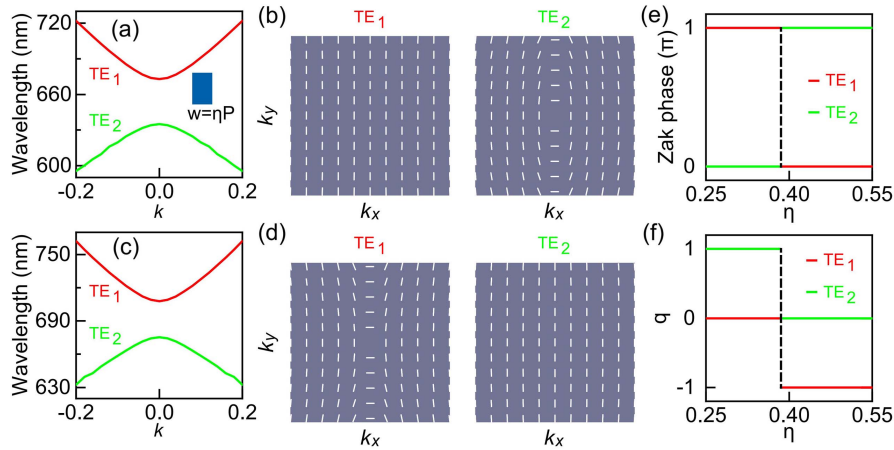


Fig. 2. Probing phase transition of band topology via radiation topology for optical analogs of the SSH model. The designed one-dimensional photonic crystal is shown in the inset of (a) and Fig. 6 in Appendix A. P is the lattice period. w is the width of the SiO₂ rectangular rod. The background medium is air. (a), (c) Band structures for $\eta = 0.3$ in (a) and $\eta = 0.45$ in (c). (b), (d) Far-field polarizations for the band structures in (a) and (c), respectively. (e) Evolution of Zak phase with η . (f) Evolution of topological charge q with η . The units of k , k_x , and k_y are all π/P . The ranges of k_x and k_y are from -0.1 to 0.1 . The black dotted line in (e), (f) is the η corresponding to the bandgap closure at Γ point.

geometric phase associated with the wavefunctions in periodic systems, playing a significant role in understanding the topological properties of materials. The value of the Zak phase is either zero or π if the systems have spatial inversion symmetry. Figures 2(a) and 2(c) are the band structures for $\eta = 0.3$ and $\eta = 0.45$, respectively. η is the structural parameter of the high dielectric constant part [see the blue part in Figs. 2(a) and 6], which determines the ratio of the inter- and intra-coupling strengths. Here, the inter- and intra-coupling strengths are equal for $\eta = 0.3845$ in Figs. 2(e) and 2(f). Thus, the band crossings occur for $\eta = 0.3845$; see Fig. 7(c) in Appendix A. Figures 2(b) and 2(d) are the far-field polarizations for the band structure in Figs. 2(a) and 2(c), respectively. The Zak phases for the TE₁ and TE₂ bands in Fig. 2(a) are π and zero, respectively. The value of q is equal to zero and $+1$ for the TE₁ and TE₂ bands in Fig. 2(a), respectively. The Zak phases for the TE₁ and TE₂ bands in Fig. 2(c) are zero and π , respectively. In such case, the band topology of the TE₁ and TE₂ bands undergoes a topological phase transition when η increases from 0.3 to 0.45. Interestingly, we can see that q also changes from zero to -1 (from $+1$ to zero) for TE₁ (TE₂) band when the band topology undergoes a topological phase transition. We further study the evolution of the Zak phase [see Fig. 2(e)] and q [see Fig. 2(f)] with η . The results in Figs. 2(e) and 2(f) clearly show that the phase transitions of the band topology and radiation topology are associated. Thus, the proposed criterion can be applied to probe the phase transition of the SSH model realized in optical systems. However, this scheme cannot be generalized to valley photonic systems because valley photonic systems are studied below the light cone without far-field radiation. The half-integer topological charges can relate to a Berry phase of π [53].

It should be noted that the total topological charge q of the four TE bands is conserved after band inversion in Fig. 1. However, the total topological charge q of the two TE bands

is not conserved after band inversion in Fig. 2. This observation is different from the previous view that the total topological charge q is conserved during its evolution [4,32,35,40]. The allowed topological charge for the representation A of the systems with C_2 symmetry is ± 1 . The topological charge carried by the representation A depends on the ratio of the inter- and intra-coupling strengths; see Figs. 2(e) and 2(f). When the intra-coupling strength is greater than the inter-coupling strength, the topological charge of representation A changes from $+1$ to -1 .

Finally, we perform experimental verification in optical analogs of the QSHEs. We fabricate the proposed band topologically trivial ($R = 148$ nm) and non-trivial ($R = 175.5$ nm) lattices based on SiN_x PhCSs and test them by our homemade 4f spectroscopy system [54,55]. The scanning electron microscopy (SEM) images and measured photonic dispersions for $R = 148$ nm and $R = 175.5$ nm samples are shown in Figs. 3(a) and 3(d), respectively. The plotted data are the photoluminescence (PL) intensities of the SiN_x PhCSs as a function of the in-plane wave vector and wavelength. It displays that the experimental results show good agreement with the calculation depicted in Figs. 1(a) and 1(d), except only with a slight wavelength difference.

To manifest the radiation topology around Γ point, we measure the polarization-resolved isofrequency contours with band-pass filters (~ 10 nm bandwidth) for two center wavelengths (CWLs) of $\lambda = 620$ and 640 nm. The measured isofrequency contours at four polarization angles of 0° , 45° , 90° , and 135° are shown in Figs. 3(b) and 3(c) for $R = 148$ nm and Figs. 3(e) and 3(f) for $R = 175.5$ nm. The polarization angle is the orientation of the polarizer's axis relative to the horizontal plane. With C_2 symmetry in our structures, the polarization states of these Bloch modes are almost linear [32,39]. When the far-field polarization azimuths of certain states are not perpendicular to the polarizer, the signal at such points will be transmitted,

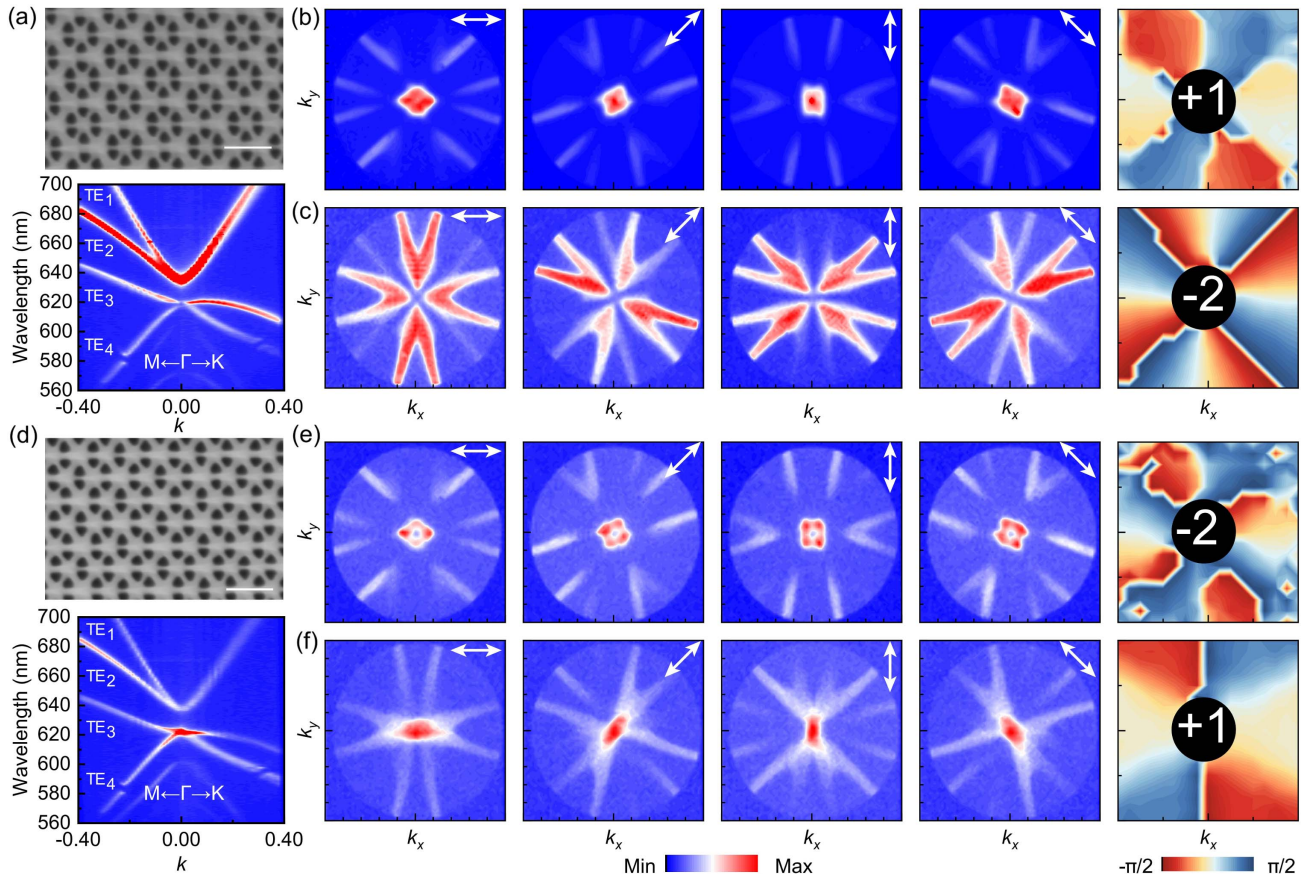


Fig. 3. SEM image and band dispersions of the band topologically trivial lattice $R = 148$ nm in (a) and non-trivial lattice $R = 175.5$ nm in (d). Polarization-resolved summed isofrequency contours and the corresponding Stokes phase maps of band topologically trivial lattice in (b), (c) and non-trivial lattice in (e), (f). The filtered center wavelengths in (b), (e) and (c), (f) are 640 nm and 620 nm, respectively. The 10 nm filter bandwidth in (b), (c) and (e), (f) is marked in Figs. 8(a) and 8(b) (Appendix A). The scale bar of SEM images is 500 nm. White arrows in the isofrequency contours denote the direction of the linear polarizer. The units of k and k_x (k_y) are $2\pi/P$. The ranges of k_x and k_y are from -0.4 to 0.4 for isofrequency contours, and from -0.08 to 0.08 for Stokes phase maps. The number in the Stokes phase map is the topological charge of radiation topology.

appearing as bright patterns. Thus, the pattern rotates along with the polarizer when the polarization vortex is present, which gives a vivid picture of the winding of far-field polarization vectors [50,53]. On the other hand, the quantitative method to determine the topological charge is to see the distributions of the Stokes phase $\phi(\mathbf{k}_{\parallel})$ defined by Eq. (3) in momentum space. Here, in experiments, the Stokes phase can be obtained by measuring the PL intensities at four polarization angles of I_{0° , I_{45° , I_{90° , and I_{135° to determine the Stokes parameters $S_1 = \frac{I_{0^\circ} - I_{90^\circ}}{I_{0^\circ} + I_{90^\circ}}$ and $S_2 = \frac{I_{45^\circ} - I_{135^\circ}}{I_{45^\circ} + I_{135^\circ}}$ [56].

For the lattice with trivial band topology, there is a bright spot around the Γ point for the 640 nm-CWL filtered spectra in Fig. 3(b). It is because the band dispersions between TE_1 and TE_2 bands have tiny differences around the Γ point and the far-field polarizations of the two bands are orthogonal [see Figs. 1(a) and 1(b)]. However, we can see the far-field polarizations that spin with the rotation of the polarizer, as shown in Fig. 3(b), which indicates the existence of a polarization vortex for $TE_{1/2}$ band in Fig. 3(a). We also give the distributions of $\phi(\mathbf{k}_{\parallel})$ in momentum space. The Stokes phase in

Fig. 3(b) experiences a $+2\pi$ change along a closed loop in the counter-clockwise direction, which clearly shows that $TE_{1/2}$ band in Fig. 3(a) has a polarization vortex at Γ point, and q is $+1$. The 620 nm-CWL filtered spectra have four clear lobes with a dark core in Fig. 3(c), because the dispersions of TE_3 and TE_4 bands are separated. In such a case, the Stokes phase accumulates -4π counter-clockwise in a closed loop, compatible with the situation of $q = -2$. The experimental results also confirm that the radiation topology of the band can be non-trivial when its band topology is trivial.

For the lattice with non-trivial band topology, similar analyses could apply to the results in Figs. 3(e) and 3(f), in which the topological charges q are -2 and $+1$ for Figs. 3(e) and 3(f), respectively. The topological charges around the Γ point are swapped between $TE_{1/2}$ and $TE_{3/4}$ bands when the band topology undergoes a topological phase transition. These experimental results provide the solid evidences that radiation topology is a more straightforward way to access the phase transitions of band topology.

3. CONCLUSION

In summary, we theoretically analyze and experimentally verify that one can probe the phase transition of band topology via radiation topology. Compared to a previous bulk-boundary correspondence principle that requires the formation of domain walls, the proposed radiation topology scheme measures the topological properties of band topology without domain walls. Moreover, such approach can also be applied to more general situations where the crystal has no full bandgap [see Figs. 3(a) and 3(d)] or topological states (see Fig. 7). Besides, since the polarization vortex is a topological configuration that is insensitive to the changes of the external environment, the radiation topology can provide a stable way to measure the phase transition of band topology. In addition, we also found that the band inversion of near-field Bloch states could provide a new way to manipulate far-field radiation. Our research not only provides an insightful understanding between band

topology and radiation topology, but also will boost the development of topological photonics, bringing essential promotion to many key applications, including tunable topological charge vortex lasers, polarization control, topological light emissions, etc.

APPENDIX A

Figures 4 and 5 show the schematics and Stokes phase maps of the photonic crystal slab used in Fig. 1. Figure 6 shows the schematic of the photonic crystal slab used in Fig. 2. The field distributions, band inversion process, and topological responses of the domain wall in Fig. 2 are exhibited in Fig. 7. The measured photonic dispersions of the filters in Fig. 3, with 10 nm bandwidth, are shown in Fig. 8.

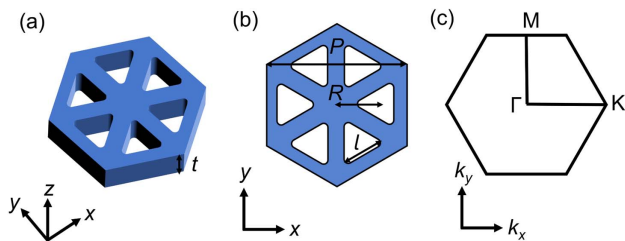


Fig. 4. (a), (b) Schematic of a graphene-like SiN_x PhCS with a hexagonal lattice of etched triangular air holes in Fig. 1. The PhCS is immersed in the air background. The thickness and lattice period of the PhCS are $t = 100$ nm and $P = 496$ nm, respectively. All triangular air holes have a side length of $l = 150$ nm and a fillet of 25 nm. R is the distance from the center of the triangular air hole to the center of the unit cell. (c) Brillouin zone of the PhCS in (a).

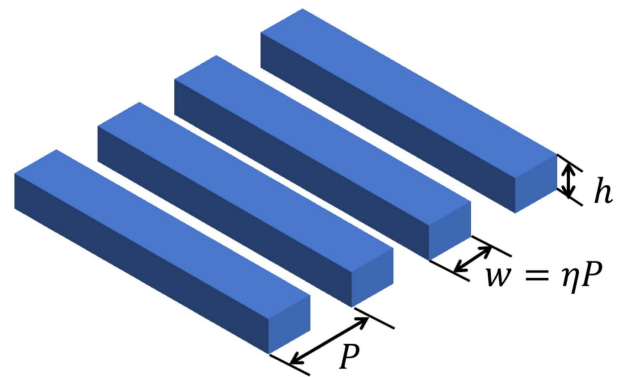


Fig. 6. Designed one-dimensional photonic crystal is used to realize the well-known Su-Schrieffer-Heeger (SSH) model. P is the lattice period. h is the thickness of the SiO₂ rectangular rod. $h = 530$ nm. w is the width of the SiO₂ rectangular rod. The background medium is air.

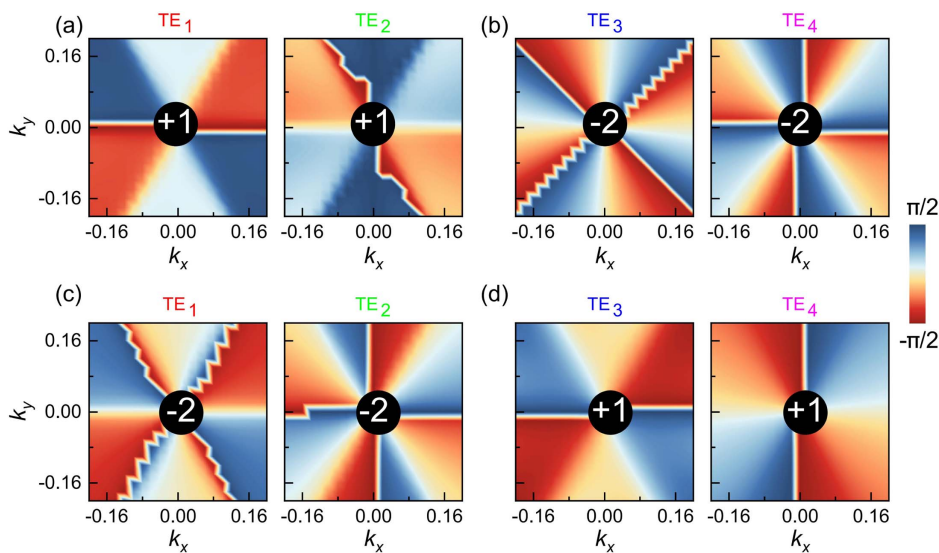


Fig. 5. Stokes phase maps for the transverse electric (TE)-like photonic bands in Fig. 1. (a), (b) Stokes phase maps for the band topologically trivial lattice $R = 148$ nm in Fig. 1(a). (c), (d) Stokes phase maps for the band topologically non-trivial lattice $R = 175.5$ nm in Fig. 1(d). The units of k_x and k_y are π/P . The number in the Stokes phase map is the topological charge of radiation topology. The band inversion mechanism can serve as an important route to explore the dynamics of topological polarization singularity and manipulate the state of polarization in the far field.

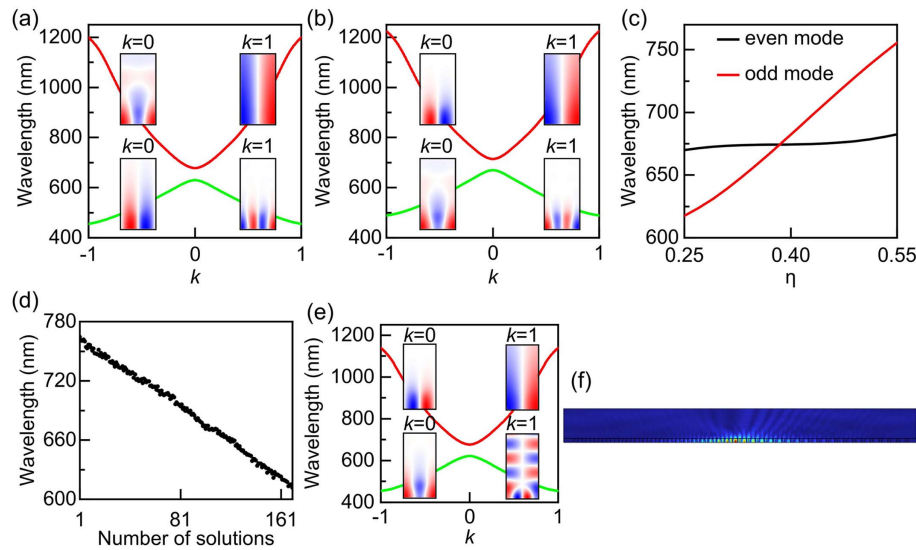


Fig. 7. P is equal to 600 nm for the results in (a)–(d). (a), (b) Band structures for $\eta = 0.3$ in (a) and $\eta = 0.45$ in (b). The structural parameters in (a) and (b) are the same as Figs. 2(a) and 2(c) in the main text, respectively. The insets in (a), (b), (e) are the field distributions of the y component of the electric field in the upper half space. (c) Illustration of band inversion process between odd and even modes at Γ point with increasing η . (d) Photonic eigenmodes of the supercell with sample size 15×15 [15 lattices for the structure in (a) and 15 lattices for the structure in (b)]. (e) Band structure for $w = 270$ nm and $P = 550$ nm. (f) Mode distributions for the edge state with sample size 15×15 [15 lattices for the structure in (a) and 15 lattices for the structure in (e)]. We have looked at the mode distribution corresponding to each eigenvalue and find no topological state on the domain wall [see (d)]. When the photonic structures on both sides of the domain wall share a common bandgap, we can clearly see the topological state on the domain wall; see (a), (e), (f). In fact we usually judge the topological phase transition of band topology experimentally by measuring whether there are topological states on the domain wall of the sample. However, this approach is very difficult to probe band topological transitions when the topologically inequivalent materials on both sides of the domain wall do not have a common bandgap. This is due to the fact that in this case there may be no topological states on the domain wall. However, the radiative topology scheme presented here directly measures the evolution of the properties of the bulk Bloch states along with the parameters without measuring the responses of the domain wall of the sample. Therefore, our method can provide another powerful tool to probe band topological transitions and may facilitate researchers to experimentally discover and realize new optical topological materials.

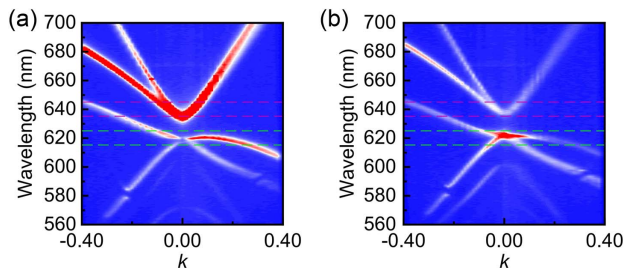


Fig. 8. Experimentally measured band dispersions of the band topologically trivial lattice in (a) and non-trivial lattice in (b). The band dispersions of (a) and (b) are the same as Figs. 3(a) and 3(d), respectively. The 10 nm filter bandwidths in Figs. 3(b), 3(c), 3(e), and 3(f) are marked with purple (640 ± 5 nm) and green (620 ± 5 nm) dotted areas in (a), (b).

Funding. National Key Research and Development Program of China (2021YFA1400700); National Natural Science Foundation of China (12321004, 12234003).

Disclosures. The authors declare no competing financial interest.

Data Availability. Data underlying the results presented in this paper are available upon reasonable request.

REFERENCES

1. L. Lu, J. D. Joannopoulos, and M. Soljačić, "Topological photonics," *Nat. Photonics* **8**, 821–829 (2014).
2. T. Ozawa, H. M. Price, A. Amo, *et al.*, "Topological photonics," *Rev. Mod. Phys.* **91**, 015006 (2019).
3. G.-J. Tang, X.-T. He, F.-L. Shi, *et al.*, "Topological photonic crystals: physics, designs, and applications," *Laser Photonics Rev.* **16**, 2100300 (2022).
4. X. Yin and C. Peng, "Manipulating light radiation from a topological perspective," *Photonics Res.* **8**, B25–B38 (2020).
5. W. Liu, W. Liu, L. Shi, *et al.*, "Topological polarization singularities in metaphotonics," *Nanophotonics* **10**, 1469–1486 (2021).
6. F. Wang, X. Yin, Z. Zhang, *et al.*, "Fundamentals and applications of topological polarization singularities," *Front. Phys.* **10**, 198 (2022).
7. F. Haldane and S. Raghu, "Possible realization of directional optical waveguides in photonic crystals with broken time-reversal symmetry," *Phys. Rev. Lett.* **100**, 013904 (2008).
8. Z. Wang, Y. Chong, J. D. Joannopoulos, *et al.*, "Observation of unidirectional backscattering-immune topological electromagnetic states," *Nature* **461**, 772–775 (2009).
9. X.-T. He, E.-T. Liang, J.-J. Yuan, *et al.*, "A silicon-on-insulator slab for topological valley transport," *Nat. Commun.* **10**, 872 (2019).
10. M. Hafezi, E. A. Demler, M. D. Lukin, *et al.*, "Robust optical delay lines with topological protection," *Nat. Phys.* **7**, 907–912 (2011).
11. M. A. Bandres, S. Wittek, G. Harari, *et al.*, "Topological insulator laser: experiments," *Science* **359**, eaar4005 (2018).
12. Y. Zeng, U. Chattopadhyay, B. Zhu, *et al.*, "Electrically pumped topological laser with valley edge modes," *Nature* **578**, 246–250 (2020).
13. I. Amelio and I. Carusotto, "Theory of the coherence of topological lasers," *Phys. Rev. X* **10**, 041060 (2020).

14. Y. Chen, X.-T. He, Y.-J. Cheng, *et al.*, "Topologically protected valley-dependent quantum photonic circuits," *Phys. Rev. Lett.* **126**, 230503 (2021).
15. W. Zhang, X. Chen, Y. V. Kartashov, *et al.*, "Finite-dimensional bistable topological insulators: from small to large," *Laser Photonics Rev.* **13**, 1900198 (2019).
16. L. J. Maczewsky, M. Heinrich, M. Kremer, *et al.*, "Nonlinearity-induced photonic topological insulator," *Science* **370**, 701–704 (2020).
17. M. Li, I. Sinev, F. Benimetskiy, *et al.*, "Experimental observation of topological Z_2 exciton-polaritons in transition metal dichalcogenide monolayers," *Nat. Commun.* **12**, 4425 (2021).
18. W. Liu, Z. Ji, Y. Wang, *et al.*, "Generation of helical topological exciton-polaritons," *Science* **370**, 600–604 (2020).
19. S. Guddala, F. Komissarenko, S. Kiriushechkina, *et al.*, "Topological phonon-polariton funneling in midinfrared metasurfaces," *Science* **374**, 225–227 (2021).
20. M. Z. Hasan and C. L. Kane, "Colloquium: topological insulators," *Rev. Mod. Phys.* **82**, 3045–3067 (2010).
21. D. Xiao, M.-C. Chang, and Q. Niu, "Berry phase effects on electronic properties," *Rev. Mod. Phys.* **82**, 1959–2007 (2010).
22. C.-K. Chiu, J. C. Teo, A. P. Schnyder, *et al.*, "Classification of topological quantum matter with symmetries," *Rev. Mod. Phys.* **88**, 035005 (2016).
23. Z.-G. Chen, C. Xu, R. Al Jahdali, *et al.*, "Corner states in a second-order acoustic topological insulator as bound states in the continuum," *Phys. Rev. B* **100**, 075120 (2019).
24. Z. Hu, D. Bongiovanni, D. Jukić, *et al.*, "Nonlinear control of photonic higher-order topological bound states in the continuum," *Light Sci. Appl.* **10**, 164 (2021).
25. Z. Guo, J. Jiang, H. Jiang, *et al.*, "Observation of topological bound states in a double Su-Schrieffer-Heeger chain composed of split ring resonators," *Phys. Rev. Res.* **3**, 013122 (2021).
26. Y. Wang, B.-Y. Xie, Y.-H. Lu, *et al.*, "Quantum superposition demonstrated higher-order topological bound states in the continuum," *Light Sci. Appl.* **10**, 173 (2021).
27. M. A. Gorlach, X. Ni, D. A. Smirnova, *et al.*, "Far-field probing of leaky topological states in all-dielectric metasurfaces," *Nat. Commun.* **9**, 909 (2018).
28. Z.-K. Lin, Y. Wu, B. Jiang, *et al.*, "Topological Wannier cycles induced by sub-unit-cell artificial gauge flux in a sonic crystal," *Nat. Mater.* **21**, 430–437 (2022).
29. M. Serra-Garcia, "Topological properties that can be heard," *Nat. Mater.* **21**, 385–386 (2022).
30. W. Gao, B. Yang, M. Lawrence, *et al.*, "Photonic Weyl degeneracies in magnetized plasma," *Nat. Commun.* **7**, 12435 (2016).
31. H. Cheng, W. Gao, Y. Bi, *et al.*, "Vortical reflection and spiraling Fermi arcs with Weyl metamaterials," *Phys. Rev. Lett.* **125**, 093904 (2020).
32. B. Zhen, C. W. Hsu, L. Lu, *et al.*, "Topological nature of optical bound states in the continuum," *Phys. Rev. Lett.* **113**, 257401 (2014).
33. C. W. Hsu, B. Zhen, A. D. Stone, *et al.*, "Bound states in the continuum," *Nat. Rev. Mater.* **1**, 16048 (2016).
34. W. Liu, B. Wang, Y. Zhang, *et al.*, "Circularly polarized states spawning from bound states in the continuum," *Phys. Rev. Lett.* **123**, 116104 (2019).
35. Y. Zeng, G. Hu, K. Liu, *et al.*, "Dynamics of topological polarization singularity in momentum space," *Phys. Rev. Lett.* **127**, 176101 (2021).
36. W. Ye, Y. Gao, and J. Liu, "Singular points of polarizations in the momentum space of photonic crystal slabs," *Phys. Rev. Lett.* **124**, 153904 (2020).
37. J. Jin, X. Yin, L. Ni, *et al.*, "Topologically enabled ultrahigh-Q guided resonances robust to out-of-plane scattering," *Nature* **574**, 501–504 (2019).
38. M. Kang, S. Zhang, M. Xiao, *et al.*, "Merging bound states in the continuum at off-high symmetry points," *Phys. Rev. Lett.* **126**, 117402 (2021).
39. M. Kang, L. Mao, S. Zhang, *et al.*, "Merging bound states in the continuum by harnessing higher-order topological charges," *Light Sci. Appl.* **11**, 228 (2022).
40. T. Yoda and M. Notomi, "Generation and annihilation of topologically protected bound states in the continuum and circularly polarized states by symmetry breaking," *Phys. Rev. Lett.* **125**, 053902 (2020).
41. X. Yin, J. Jin, M. Soljačić, *et al.*, "Observation of topologically enabled unidirectional guided resonances," *Nature* **580**, 467–471 (2020).
42. G. Salerno, R. Heilmann, K. Arjas, *et al.*, "Loss-driven topological transitions in lasing," *Phys. Rev. Lett.* **129**, 173901 (2022).
43. L.-H. Wu and X. Hu, "Scheme for achieving a topological photonic crystal by using dielectric material," *Phys. Rev. Lett.* **114**, 223901 (2015).
44. Y. Yang, Y. F. Xu, T. Xu, *et al.*, "Visualization of a unidirectional electromagnetic waveguide using topological photonic crystals made of dielectric materials," *Phys. Rev. Lett.* **120**, 217401 (2018).
45. S. Barik, A. Karasahin, C. Flower, *et al.*, "A topological quantum optics interface," *Science* **359**, 666–668 (2018).
46. N. Parappurath, F. Alpeggiani, L. Kuipers, *et al.*, "Direct observation of topological edge states in silicon photonic crystals: spin, dispersion, and chiral routing," *Sci. Adv.* **6**, eaaw4137 (2020).
47. W. Liu, M. Hwang, Z. Ji, *et al.*, " Z_2 photonic topological insulators in the visible wavelength range for robust nanoscale photonics," *Nano Lett.* **20**, 1329–1335 (2020).
48. D. Smirnova, S. Kruk, D. Leykam, *et al.*, "Third-harmonic generation in photonic topological metasurfaces," *Phys. Rev. Lett.* **123**, 103901 (2019).
49. S. Arora, T. Bauer, N. Parappurath, *et al.*, "Breakdown of spin-to-helicity locking at the nanoscale in topological photonic crystal edge states," *Phys. Rev. Lett.* **128**, 203903 (2022).
50. Y. Zhang, A. Chen, W. Liu, *et al.*, "Observation of polarization vortices in momentum space," *Phys. Rev. Lett.* **120**, 186103 (2018).
51. J. K. Asbóth, L. Oroszlány, and A. Pályi, *A Short Course on Topological Insulators* (Springer, 2016), Vol. **919**, p. 166.
52. M. Xiao, Z. Zhang, and C. T. Chan, "Surface impedance and bulk band geometric phases in one-dimensional systems," *Phys. Rev. X* **4**, 021017 (2014).
53. A. Chen, W. Liu, Y. Zhang, *et al.*, "Observing vortex polarization singularities at optical band degeneracies," *Phys. Rev. B* **99**, 180101 (2019).
54. W. Lan, P. Fu, C.-Y. Ji, *et al.*, "Visualization of photonic band structures via far-field measurements in $\sin x$ photonic crystal slabs," *Appl. Phys. Lett.* **122**, 151102 (2023).
55. R. Wagner, L. Heerklotz, N. Kortenbruck, *et al.*, "Back focal plane imaging spectroscopy of photonic crystals," *Appl. Phys. Lett.* **101**, 081904 (2012).
56. G. J. Gbur, *Singular Optics* (CRC Press, 2016).